Operando AC In-Plane Impedance Spectroscopy of Electrodes for Energy Storage Systems

Victor Maurel, Kevin Brousse, Tyler Mathis, Audrey Perju, Pierre-Louis Taberna, Patrice Simon

Journal of The Electrochemical Society, 2022 **169** 120510

Operando AC In-Plane Impedance Spectroscopy of Electrodes for Energy Storage Systems

Victor Maurel,[1,2] Kevin Brousse,[1,2] Tyler S. Mathis,[1,2] Audrey Perju,[1] Pierre-Louis Taberna,[1,2,z] and Patrice Simon[1,2,z]

[1] *Université de Toulouse III Paul Sabatier, CIRIMAT UMR CNRS 5085, 118, Route de Narbonne, 31062 Toulouse cedex 9, France*
[2] *Réseau sur le Stockage Electrochimique de l'Energie (RS2E) FR CNRS, 3459, Amiens, France*

Characterization of battery and supercapacitor materials and devices is typically performed using various methods such as cyclic voltammetry, electrochemical impedance spectroscopy, galvanostatic cycling, etc. However, none of these techniques allow for operando tracking of changes in the electrode material's in-plane ionic and electronic percolation under polarization, which plays a key-role in the electrochemical performance of the material. Here, we report an experimental set-up devoted to measuring the operando in-plane AC impedance and DC resistance of porous activated carbon and Ti_3C_2 MXene electrodes during electrochemical cycling. These impedance measurements allow for the deconvolution and tracking of the ionic and electronic contributions of the total impedance and the change in these components under polarization. Operando tracking of the in-plane electrode impedance under polarization brings insights regarding electronic and ionic transport mechanisms of electrodes during operation. This set-up serves as a complementary tool to further evaluate and improve the performance of electrode materials for energy storage.

 [DOI: 10.1149/1945-7111/aca723]

Manuscript submitted October 3, 2022; revised manuscript received November 8, 2022. Published December 13, 2022.

Supplementary material for this article is available online

It is well known that electronic and ionic conductivity are two of the most important electrode material parameters that influence the efficiency of batteries and supercapacitors.[1] A good understanding of the electronic and ionic transport properties at electrode/electrolyte interfaces is crucial for the design and manufacturing of high-performance electrodes for energy storage systems.

Several methods exist to investigate the performance and characteristics of electrode/electrolyte systems. Cyclic voltammetry (CV), impedance spectroscopy (EIS), and galvanostatic cycling are the most commonly used methods for studying the electrochemical behavior of electrode materials and energy storage devices.[2,3] Performing physical characterization techniques in tandem with electrochemical cycling enables investigation of the micro-, or even nano-scale changes occurring in electrode materials during electrochemical reactions. For example, in situ X-ray diffraction (XRD) is a convenient method for tracking phase changes and structural deformation in battery-like electrodes[4] and for monitoring interlayer spacing changes occurring in capacitive, two-dimensional (2D) materials like graphene or MXenes.[5,6] Techniques and instruments that can directly probe electrochemical interfaces, like the electrochemical quartz crystal microbalance (EQCM) and scanning electrochemical microscopy (SECM), provide information about ion/solvent adsorption and charge transfer mechanisms occurring at electrode/electrolyte interfaces.[7–9]

However, to the best of our knowledge, there have been only few in-plane impedance studies, limited by the cell set-up to electrochemically prepared materials like conducting polymers,[10] but no attempts to date at recording the changes in in-plane impedance during the charging and discharging processes of an electrode used for electrochemical energy storage. More surprising is the minimal number of reports available concerning the changes in in-plane resistivity of metal-like conductive films under bias potential. According to Tucceri et al. in 1981, changes in resistivity can be attributed to two phenomena: (1) changes in the concentration of charge carriers in the electrode material, and (2) the formation of adsorptive bonds at the electrode/electrolyte interface.[11] In 2006, Pollak et al. studied the dependence of a porous carbon electrode's resistivity on its state of charge when used as a molecular sieve.[12,13] Their results showed that decreases in the electrode's surface resistivity were correlated with the quantity of adsorbed species. Vol'fkovich et al. performed surface resistivity measurements on porous carbon electrodes used in capacitive deionization and found that electrolyte that was confined within capillary pores had lower resistivity than the surrounding, bulk electrolyte solution.[14] Andrew P. Saab et al. measured the in-plane impedance of a carbon/polyelectrolyte Fuel-Cell composite electrode, and highlighted the existence of two parallel ways for transport properties depending on the frequency range, one ionic at high frequencies, and one electronic at low frequency.[15] On the other hand, significant resistivity changes were observed during polarization for monolayer CVD graphene and multilayer CVD graphene.[16,17]

Until now, surface resistance measurements performed under bias have been made mainly using direct current (DC) with the van der Pauw (VdP) method.[18–20] The VdP method gives information about the overall resistance of an electrode along a direction parallel to the electrode surface (in-plane), however it is not possible to isolate the ionic and electronic contributions of the resistivity change. To address this point, we have developed an original methodology to perform operando and in-plane impedance thanks to the combined use of alternating current (AC) and the VdP method. The combination of AC and the VdP method allows for the measurement of the in-plane electrode impedance under different potentials and, more importantly, enables deconvolution of the ionic and electronic contributions to the total electrode resistivity depending on the frequency range.

In the present work, the electronic and ionic in-plane transport properties of two different materials used for energy storage applications were studied operando (during electrochemical cycling): a porous activated carbon (YP50F), widely used for capacitive energy storage,[21,22] thanks to its decent conductivity (70 $S.cm^{-1}$),[23,24] high surface area and pore size distribution,[25,26] and the MXene Ti_3C_2. MXenes are 2D transition-metal carbides, nitrides, and carbonitrides which can achieve high conductivity (>20,000 $S.cm^{-1}$)[27,28] and extremely fast proton intercalation redox reactions in acidic electrolytes.[29]

[z] E-mail: pierre-louis.taberna@univ-tlse3.fr; patrice.simon@univ-tlse3.fr

Results and Discussion

The changes in the in-plane resistivity of the electrodes under bias were measured using the electrochemical cell presented in Fig. 1a. Two different potentiostats were used to measure the in-plane impedance of the electrode at different applied potentials. The first potentiostat was used to apply a constant potential to the electrode material (Figs. 1b, 1c) until a steady-state was reached, while the second potentiostat was used to record the in-plane AC and DC impedance during the potentiostatic experiments (see also Fig. 1d). Potentiostatic experiments were firstly selected to enable recording of the AC and DC impedances at a steady-state, and to minimize any residual current originating from polarization, which can interfere with the measurement current, especially for the AC measurements (see Supplementary Figs. S1–S3).[12,13] In addition, the Au contact pads used for polarizing the electrode were placed symmetrically on the sample, thereby negating any potential shift across the sample (Figs. 1b and 1c). AC measurements being sensitive to the geometry of electric field,[31] this technique allows for tracking relative changes in the electrode resistances.

To highlight the contribution from the electrolyte on the transport properties of an electrode/electrolyte system, preliminary AC measurements were first performed on a $R_1 = 1$ kΩ resistor in air and when immersed in 1 M H_2SO_4 (See Supplementary Figs. S4 and S5). As expected, the impedance of the resistor in air exhibits only a real contribution—the phase angle is close to zero—of approximately 1,000 Ω. When the resistor is immersed in an electrolyte, an ionic contribution appears in the high and medium frequency ranges. This ionic resistance can be modeled using a simplified R_2-CPE_1 equivalent circuit in parallel with R_1 (1 kΩ resistor), as detailed in Supplementary Figs. S4 and S5. At high frequencies, the measured

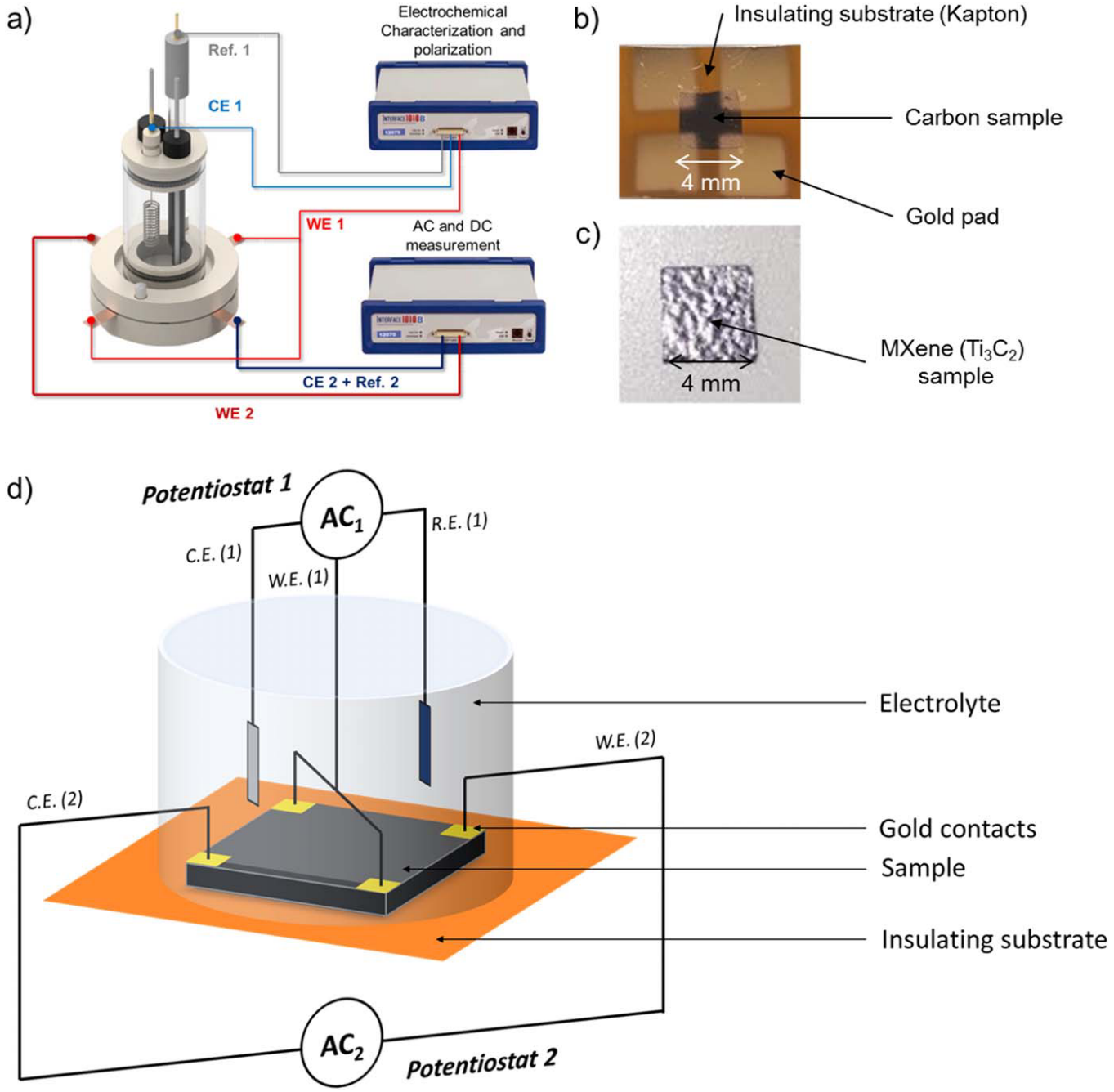

Figure 1. Experimental set-up (a) Schematic of the experimental set-up[30] used for AC and DC impedance measurements under polarization. (b) Image of a YP50F activated carbon sample with gold current collector. (c) Image of a Ti_3C_2 sample without a current collector and d) sketch of the cell set-up and electrode connection (detail of panel a).

impedance is caused by electrolyte ionic transport between the two electrodes. At low frequencies, the current flows directly through the 1 kΩ resistor, as a result of the increase of the capacitive impedance $Z' = 1/Q(j\omega)^{\alpha}$. Overall, the high frequency region of the Bode plot shows the contributions of the ionic path to the impedance and the electronic component appears in the low frequency region.

In-plane impedance of porous carbon in 1 M H_2SO_4.— Figure 2a shows a schematic of the porous YP50F carbon film coated on an electrically insulating Kapton© substrate. In-plane impedance spectroscopy measurements were made on the film, first in air (dry) and then two hours after immersion in 1 M H_2SO_4 (impregnated), as the impedance was found to be constant for longer immersion times (Supplementary Fig. S6). The optimum electrolyte volume to fill the entire electrode porosity is around 50 $ml.g^{-1}$ of carbon in the cell set-up used (Supplementary Fig. S7). As expected, the dry sample exhibits resistive behavior, with a total resistance of approximately 1.25 kΩ (Figs. 2b and 2c). After immersion in the acidic electrolyte, the impedance spectrum reveals an ionic percolation path at high frequencies, which is further short-circuited at low frequencies by the electronic path along the carbon layer.

Importantly, both the Nyquist and Bode plots (Figs. 2b and 2c) show that the low frequency resistance of the activated carbon in the electrolyte is lower than the resistance of the dry film (∼1 kΩ vs ∼1.25 kΩ, respectively). Figure 2d shows the equivalent circuit used to depict the percolation paths in the carbon electrodes during AC in-plane measurements, with an ionic branch and an electronic branch in parallel.[15] The design of the equivalent circuit together with the selection of the various components is described step-by-step (see Supplementary Figs. S8-S13). The electronic impedance branch of the porous carbon film can be modeled by a resistance, R_2, in series with a parallel CPE_1/R_3 circuit. R_2 is associated with the bulk impedance of the carbon grains, and CPE_1/R_3 represents the contact impedance between the carbon particles, where R_3 is the contact resistance and CPE_1 is the contact capacitance - a CPE was used, accounting for a slight deviation from the ideal capacitive behavior. The ionic impedance branch of the porous carbon film can be described using a Transmission Line Model (TLM), which is well known in the capacitive storage community.[2] The TLM consists of a Z_{TLM} impedance (1) in series with a resistance R_1, that describes the high frequency equivalent series ionic resistance between the W.E. 2 and C.E. 2 (Fig. 1d). R_{ion} is the in-pore ionic resistive part accorded to the transmission line model (Ω), Q is a constant phase element accounting for the capacitive storage in the transmission line model ($S.s^{\alpha}$), and L represents the normalized electrode thickness, which is set to 1. Z_{TLM} is null at high frequencies and infinite at low frequencies:

$$Z_{TLM}(\omega) = \sqrt{\frac{R_{ion}}{Q(i\omega)^{\alpha}}}\ \coth\left(L\sqrt{R_{ion}Q(i\omega)^{\alpha}}\right) \qquad [1]$$

The equivalent circuit of Fig. 2d has been used to model the impedance plots. The assignment of the ionic and electronic percolations to the high and low frequency range, respectively, was made by using electrolytes with different concentrations (Supplementary Figs. S14–S15) and electrodes of different thicknesses (Supplementary Figs. S16–S18). Results confirmed that the high frequency (AC) impedance is controlled by the ionic resistance while the low frequency (DC) impedance is driven by the electronic percolation along the electrode. The contribution of the ionic and resistive impedance branches of the porous carbon electrode was more specifically evidenced by calculating the associated admittance

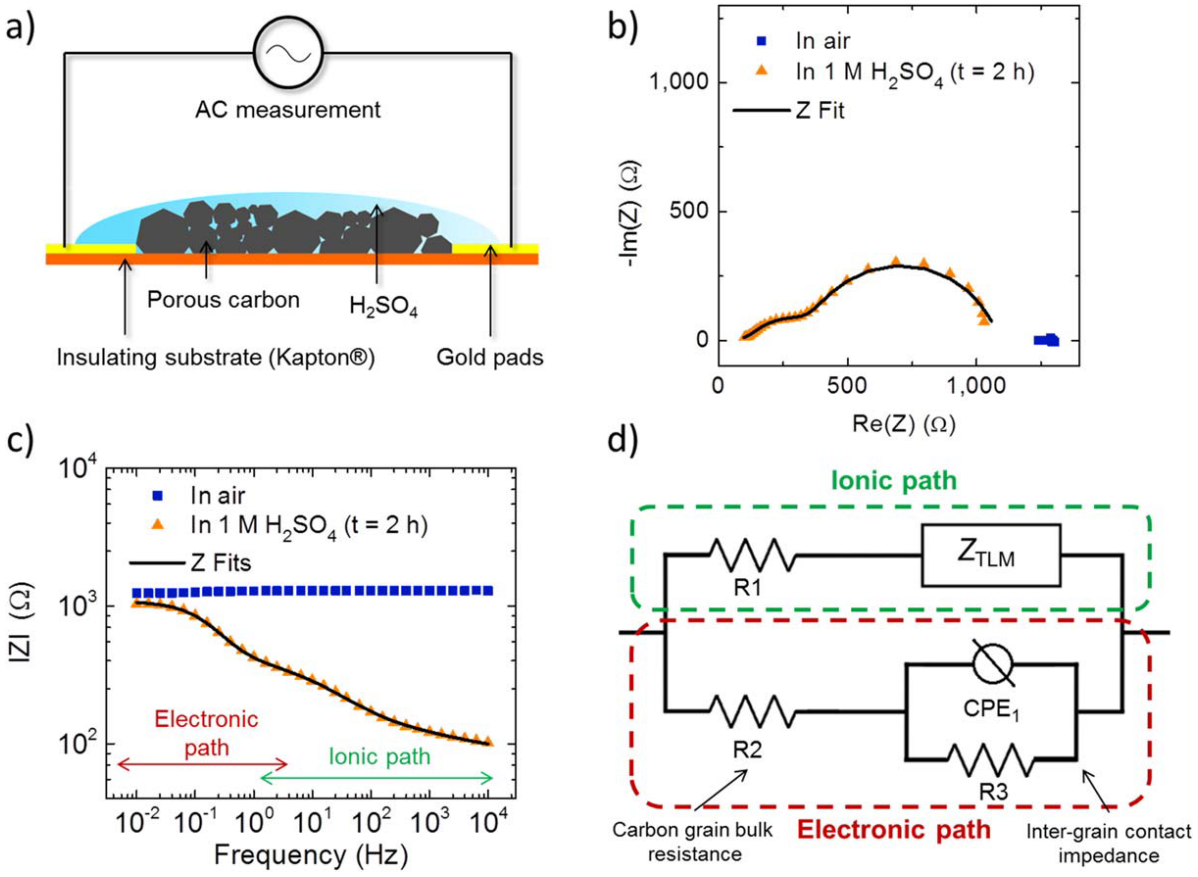

Figure 2. Highlighting the ionic and electronic paths in porous activated carbon. (a) Schematic of the experimental set-up showing the porous carbon layer on an insulating substrate immersed in 1 M H_2SO_4 electrolyte and the two Au contacts used for AC measurements. (b) Nyquist and (c) Bode plots of the AC in-plane impedance measurements for the porous carbon electrode in air (blue squares) and in 1 M H_2SO_4 electrolyte (orange triangles). (d) Equivalent circuit used to model the AC in-plane impedance of the porous carbon electrode in 1 M H_2SO_4. The results of the fits are shown as black lines in (b) and (c).

(see an example in Supplementary Fig. S14b) to quantitatively show the ionic vs electronic contributions in the electrode. Also, the Kapton substrate impedance was found to be about 5 orders of magnitude higher versus the electrode impedance and the capacitive contribution of the gold contacts was negligible, so that they do not affect the measurements (Supplementary Figs. S10–S13).

To highlight the differences between conventional out-of-plane AC impedance spectroscopy and the in-plane AC impedance spectroscopy measurements performed in this study, out-of-plane impedance spectroscopy was performed on the porous carbon electrode at open circuit potential using a three-electrode set-up. The Nyquist plot (Supplementary Fig. S19) shows the expected capacitive behavior of a porous carbon electrode, with a linear increase of the imaginary part of the impedance at low frequency as a result of the electrostatic charge storage mechanism. The out-of-plane AC impedance Nyquist plot was fitted using the above TLM model (Supplementary Fig. S20). As expected, the in-pore resistance (R_{ion}) in the out-of-plane experiments was found to be one order of magnitude smaller than the one measured during in-plane experiments, as a result of the difference in the measurements (in-plane vs out-of-plane).

The activated carbon films were then further cycled in the 1 M H_2SO_4 between −0.7 to 0.2 V vs Hg/Hg_2SO_4 using potentiostat #1 (Figs. 1a and d). The CVs are shown in Fig. 3a.

The rectangular shape of the voltammograms for the activated carbon electrode is representative of the expected capacitive behavior of the porous carbon, where charge storage occurs electrostatically due to ion adsorption on the carbon surface. The capacitance reaches approximately 290 $mF.cm^{-2}$ at 5 $mV.s^{-1}$ for the 0.16 cm^2 electrode. In-plane impedance measurements were then recorded at different applied potentials using potentiostat #2. The absence of significant changes in the high frequency impedance in the Bode (Fig. 3b) and Nyquist (Fig. 3c) plots, controlled by the ionic conductivity in highly concentrated H_2SO_4 electrolyte (see Supplementary Fig. S14), shows that the ionic percolation in the film remains roughly constant during polarization. Indeed, as shown in Fig. 3d, the electronic impedance component drives the variations in the overall impedance during polarization. A ∼60% decrease in resistance was measured when the applied potential increased from −0.7 V (1195 Ω) to 0.2 V vs Hg/Hg_2SO_4 (441 Ω). All measured resistance values for the activated carbon electrode in H_2SO_4 are presented in Table I.

The decrease of the bulk carbon grain resistance R_2 with the increase in applied potential could be due to an increase in the charge carrier density in the carbon at the electrode/electrolyte interface that results from ion adsorption under applied potential.[12,13] Supplementary Fig. S21 shows that the capacitance C_1 from CPE_1 representing the carbon grain/carbon grain interface also depends on the applied potential, as expected from the slight volume expansion of porous carbon grains that occurs during polarization.[32,33] Such volume expansion also leads to decreases in the contact resistance, R_3 (Table I). Since the substrate that the

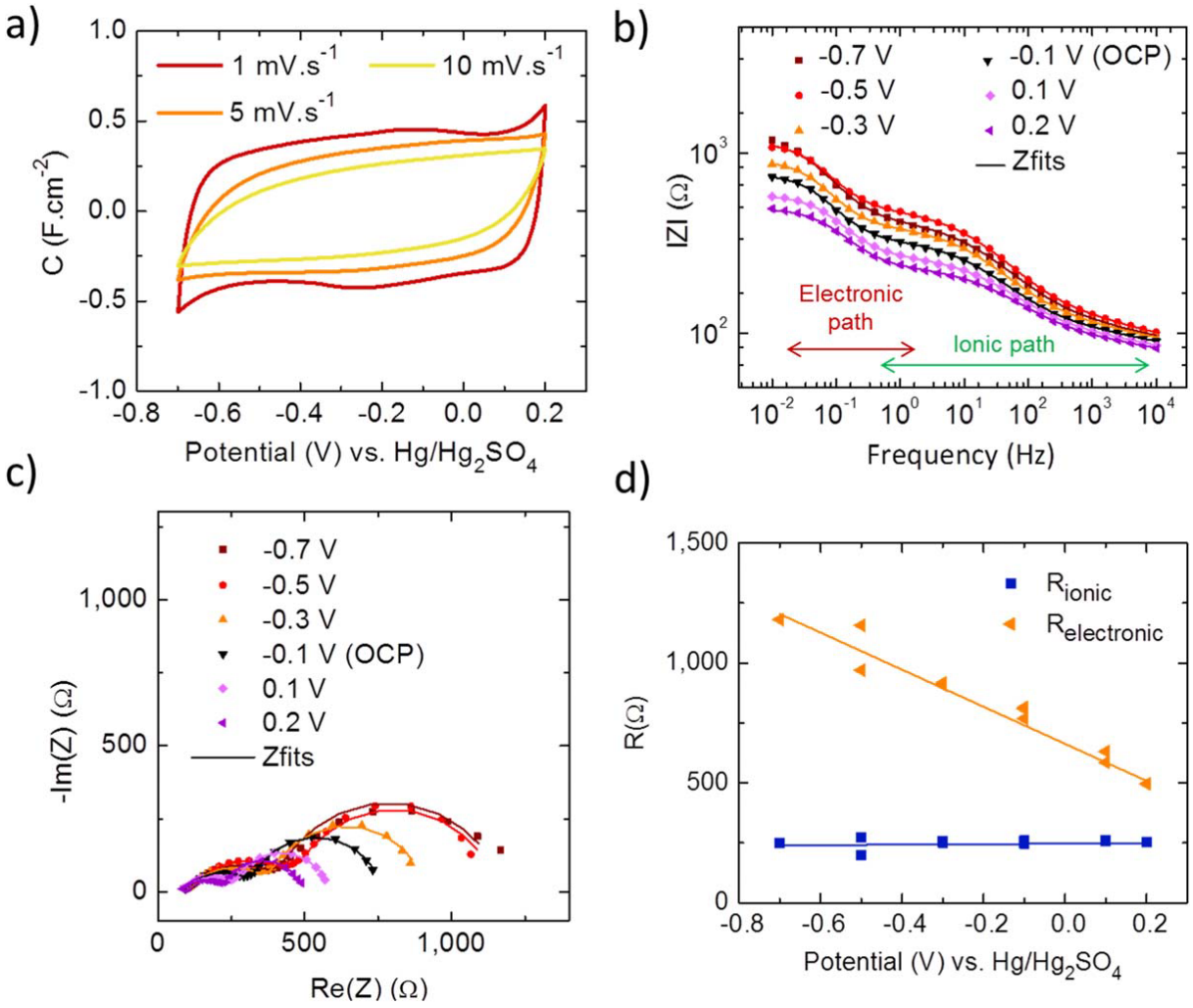

Figure 3. Electrochemical characterization of porous activated carbon. (a) Cyclic voltammetry of a 25 μm thick YP50F electrode in 1 M H_2SO_4 vs Hg/Hg_2SO_4 at 1, 5, and 10 $mV.s^{-1}$. (b) Bode plots with corresponding fit lines and (c) Nyquist plots with corresponding fit lines showing the influence that applied voltage has on the activated carbon electrode. (d) Extraction from the total resistance (R_{TOT}) of the ionic (R_{ionic}) and electronic ($R_{electronic}$) contributions according to the equivalent circuit shown in Fig. 2d.

Table I. Parameters corresponding to the impedance of activated carbon in 1 M H_2SO_4 at different applied potentials obtained by fitting the impedance data using the equivalent circuit shown in Fig. 2d. with $R_{ionic} = R_1 + R_{ION}$ and $R_{electronic} = R_2 + R_3$.

				CPE 1		TLM		
Potential (V) vs Hg/Hg_2SO_4	R_1 (Ω)	R_2 (Ω)	R_3 (Ω)	Y_1 ($S.s^a$)	a_1	R_{ION} (Ω)	Y_2 ($S.s^a$)	a_2
−0.1	88	354	461	5.21E-03	0.88	171	8.86E-05	0.66
−0.3	87	380	527	4.89E-03	0.88	164	9.64E-05	0.65
−0.5	83	443	526	4.83E-03	0.97	116	1.55E-04	0.57
−0.7	85	433	748	3.49E-03	0.85	164	8.69E-05	0.63
−0.5	86	492	665	3.96E-03	0.87	187	7.44E-05	0.65
−0.3	89	397	520	5.08E-03	0.89	169	8.65E-05	0.65
−0.1	90	335	433	5.52E-03	0.89	157	9.36E-05	0.65
0.1	88	271	315	5.47E-03	0.88	169	8.24E-05	0.66
0.2	90	235	261	5.89E-03	0.86	163	7.65E-05	0.65
0.1	86	290	341	5.05E-03	0.87	175	7.46E-05	0.66
−0.1	85	346	462	5.30E-03	0.86	168	8.93E-05	0.65

carbon is attached to is rigid, any swelling of the carbon grains would induce better contact between the carbon particles, resulting in improved electrical percolation and decreased resistance. DC resistance measurements were also performed at different potentials, by applying a constant current using potentiostat #2, and the results are plotted in Supplementary Fig. S22. The change in resistance vs applied potential from DC measurements exhibits a similar trend as the one obtained at low frequency in Fig. 2d, validating the operando mode under these operating conditions.

In-plane impedance of porous carbon in EMITFSI.—An operando AC in-plane impedance measurement was also performed using 1-Ethyl-3-methylimidazolium bis(trifluoromethylsulfonyl) imide (EMITFSI) as the electrolyte.

Figure 4a shows the expected electrochemical behavior for an activated porous carbon electrode in an ionic liquid electrolyte. A capacitance of 60 $mF.cm^{-2}$ at 10 $mV.s^{-1}$ was measured between the potential range from −1.5 V to 1.2 V vs Ag/Ag^+. In-plane impedance spectroscopy measurements were made on the film, first in air (dry) and then after one hour of immersion in neat EMITFSI electrolyte (impregnated), as the impedance was found to be constant for longer immersion times (Supplementary Fig. S6) (Fig. 4b). The in-air sample exhibited resistive behavior, with a resistance value of approximately 3 kΩ. After 2 h of immersion in EMITFSI, the Bode plot is similar to what was obtained for the H_2SO_4 electrolyte (Fig. 3b), where an ionic impedance shows up at high frequencies. The low frequency resistance, mainly driven by the electronic resistance, increases after 2 h immersion in the ionic liquid electrolyte. This change in the low frequencies range is ascribed to the presence of the ionic liquid electrolyte in the activated porous carbon electrode, which leads to a grain-grain contact resistance increase. Figure 4c presents the Bode plots obtained at different electrode polarization. The low frequency impedance varies with the polarization potential and a total change of R_{TOT} around 90% was measured between −0.5 V (10.5 kΩ) and 1.2 V vs Ag/Ag^+. (1.5 kΩ), as shown in Fig. 4d. In order to obtain more accurate results, the data was fitted using the equivalent circuit described in Fig. 2d. All measured resistance values for the activated carbon electrode in EMITFSI are listed in Table II. In contrast to the results obtained for the activated porous carbon sample in the H_2SO_4 electrolyte, where the electronic and ionic resistance followed a linear trend across the entire potential range (Fig. 3d), a symmetric decrease from 0 V vs Ag/Ag^+ was recorded for both the ionic and electronic resistance (Fig. 4d) in EMITFSI. Interestingly, as shown in Fig. 4a, this potential corresponds to the open circuit potential (OCP) of the electrode, so that both resistance variations are correlated with the charge injection and the resulting carbon doping. In 2013 Vol'fkovich et al. also reported a similar trend for the variation of an electrode resistance upon polarization, which was ascribed to a conductivity enhancement with ion confinement within the porous carbon network. A minimum of conductivity was also observed at the OCP.[14] Nevertheless, here, the influence of the volume variation cannot be fully ruled out as both ionic and electronic resistance follow the same trend as volume variation recorded by in situ dilatometry using similar activated porous carbon electrodes (See Supplementary Figs. S23 and S24).[32,33] Moreover, DC measurements were also made in dynamic mode - operando - during the CV, and not step wise at constant potential holds. Supplementary Fig. S25 shows that DC measurements achieved in operando mode are similar to those obtained under potentiostatic conditions (Fig. 4d). Those results further validate the in-plane AC measurements as a tool for the operando tracking of the in-plane electronic percolation in electrodes during charge storage.

In-plane impedance of Ti_3C_2 MXene.—In-plane impedance measurements were also applied to characterize the resistivity and impedance changes of the MXene Ti_3C_2, which exhibits strong redox behavior during electrochemical cycling. Figure 5a shows the CVs of Ti_3C_2 in 1 M H_2SO_4, where the characteristic broad redox peaks of Ti_3C_2 can be seen in the −0.5 V to −1.1 V vs Hg/Hg_2SO_4 potential region, on top of a double layer capacitive envelope, in agreement with the surface redox capacitance charge storage mechanism previously reported for this material.[29] The capacitance of the 0.16 cm^2 electrode reaches 250 $mF.cm^{-2}$ at 10 $mV.s^{-1}$. Since the electronic conductivity of the Ti_3C_2 electrode is several orders of magnitude higher than the electrolyte conductivity, only the electronic contribution to the total impedance is visible after immersion of the Ti_3C_2 electrode in the electrolyte (Fig. 5b), in agreement with the proposed equivalent circuit (Fig. 2d). The Ti_3C_2 electrode behaves like a simple resistance regardless of the presence of electrolyte (see also the Nyquist plots in Supplementary Fig. S26) - as opposed to the results for the porous carbon electrode. A slight increase in the resistance is seen following electrolyte immersion (Fig. 5b), most likely associated with the insertion of the electrolyte (water molecules) between the MXene sheets which slightly affects the electrical percolation.

As the MXene electrode only shows purely resistive behavior, DC resistance measurements are more relevant since better accuracy can be achieved. Figure 5c shows the in situ changes in electronic percolation at different applied potentials, while Fig. 5d shows the operando changes in electronic percolation during cyclic voltammetry. Both techniques shows similar changes, with a slight hysteresis for the operando mode, due to the dynamic measurement. The DC resistance for Ti_3C_2 (which is analogous to extrapolation of the low frequency impedance, where the electrical percolation can be seen) changes by approximately 28% between −0.1 V and −0.8 V vs Hg/Hg_2SO_4 (Fig. 5d).

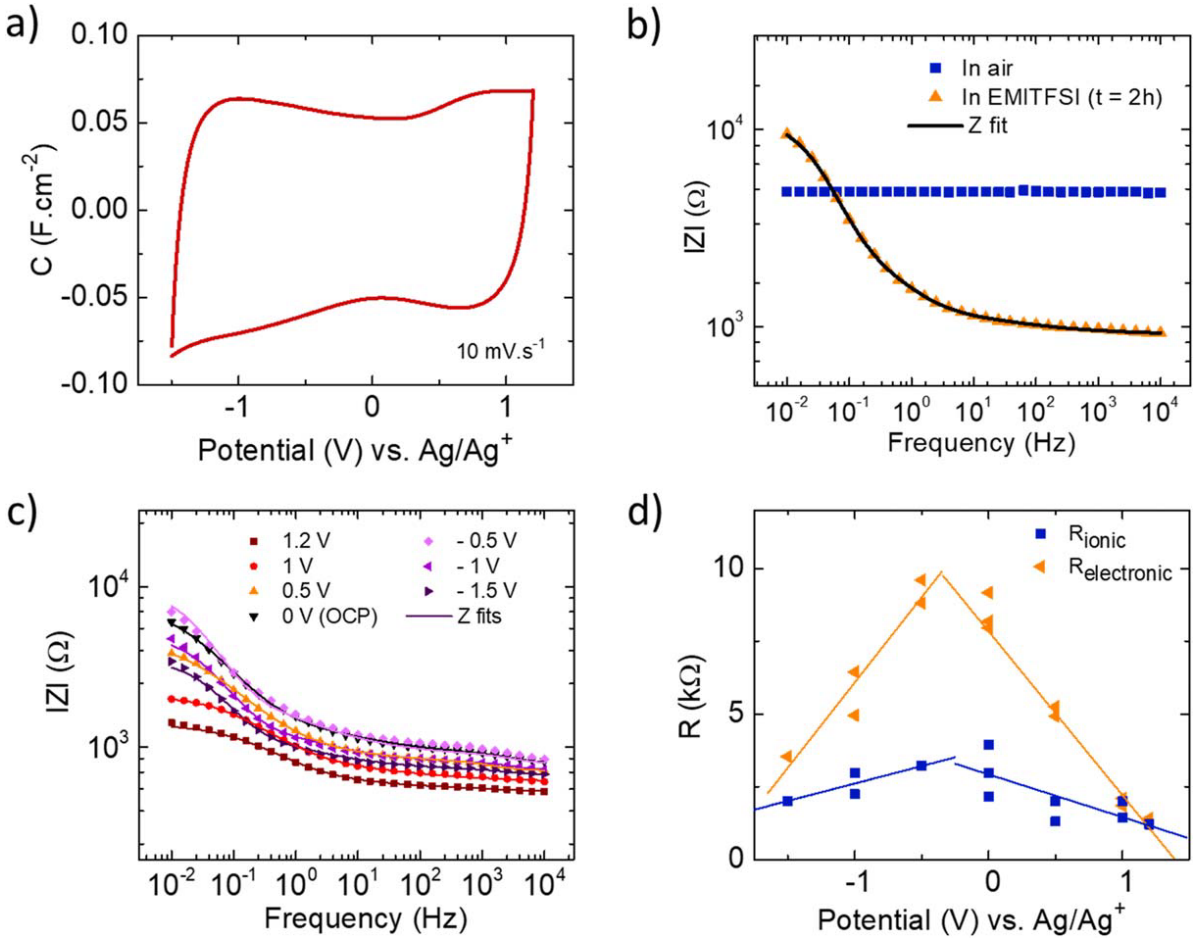

Figure 4. Electrochemical characterization of porous activated carbon in the ionic liquid EMITFSI. (a) Cyclic voltammetry of a 25 μm thick YP50F electrode in EMITFSI vs Ag/Ag^+ at 10 $mV.s^{-1}$. (b) Bode plots with corresponding fit lines of the dry and impregnated sample (c) Bode plots with corresponding fit lines showing the influence that applied voltage has on the activated carbon electrode. (d) Extraction from the total resistance (R_{TOT}) of the ionic (R_{ionic}) and electronic ($R_{electronic}$) contributions according to the equivalent circuit shown in Fig. 2.

Table II. Parameters corresponding to the impedance of activated carbon in EMITFSI at different applied potentials obtained by fitting the impedance data using the equivalent circuit shown in Fig. 2d. with $R_{ionic} = R_1 + R_{ION}$ and $R_{electronic} = R_2 + R_3$.

				CPE 1		TLM		
Potential (V) vs Ag/Ag+	R_1 (Ω)	R_2 (Ω)	R_3 (Ω)	Y_1 ($S.s^a$)	a_1	R_{ION} (Ω)	Y_2 ($S.s^a$)	a_2
0	997	4208	4954	2.66E-08	0.99	1986	4.06E-04	0.75
0.5	860	3228	2023	6.12E-08	0.61	1140	4.33E-04	0.63
1	828	1743	101	1.16E-09	0.95	622	3.67E-04	0.62
1.2	869	1256	153	4.41E-05	0.51	332	3.18E-04	0.61
1	998	1515	581	1.81E-06	0.73	1004	1.82E-04	0.66
0.5	900	3053	1865	7.97E-08	0.95	402	4.21E-04	0.59
0	967	3913	4041	2.55E-08	0.92	1194	4.05E-04	0.66
−0.5	961	4235	5360	2.16E-08	0.99	2243	5.02E-04	0.81
−1	929	3050	1898	4.07E-08	0.9	1312	5.90E-04	0.81
−1.5	888	2670	863	8.93E-08	0.99	1125	6.65E-04	0.79
−1	1038	3311	3127	3.10E-08	0.86	1927	4.97E-04	0.796
−0.5	1051	3622	5181	2.38E-08	0.95	2165	4.79E-04	0.774
0	1065	3495	4686	4.58E-08	0.88	2876	4.76E-04	0.818

Interestingly, the changes in DC resistance at different applied potentials follow the change in the charge storage mechanism from capacitive to surface redox, as the applied potential decreases (Fig. 5a). The electrical resistance of the MXene electrode reaches a minimum at the peak potential, as a result, the DC resistance change *versus* potential exhibits a parabolic shape. It is worth mentioning that similar trend was found for the change of the *c*-lattice parameter of Ti_3C_2 MXene electrode in H_2SO_4 electrolyte, where the minimum interlayer spacing values were recorded at the redox peak potentials.[34] Accordingly, it is highly likely that the changes in DC resistance for the 2D Ti_3C_2 MXene electrode *versus* potential observed during our in-plane impedance measurements is linked to the contraction/expansion of the MXene interlayer spacing due to the intercalation/de-intercalation of water molecules that

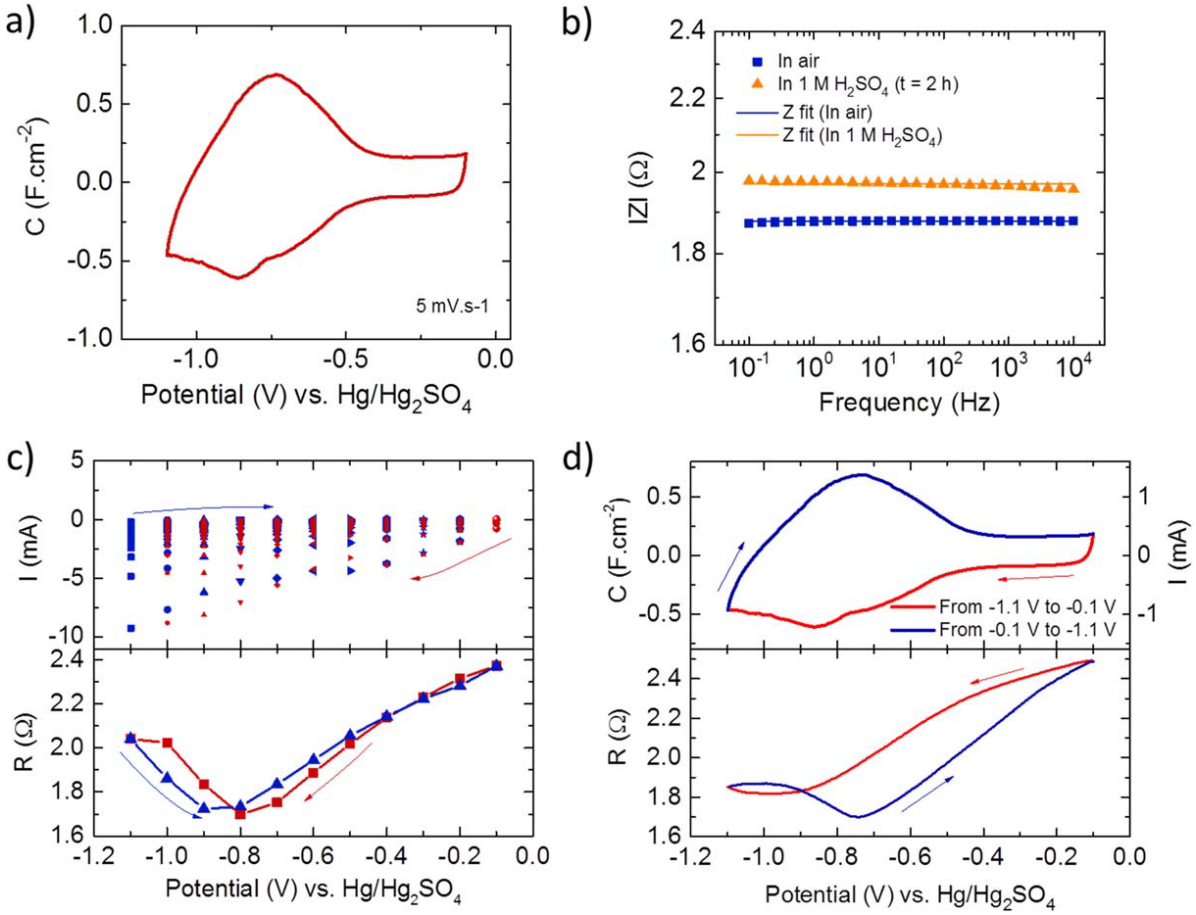

Figure 5. Characterization of Ti_3C_2 MXene using AC in-plane impedance measurements. (a) Cyclic voltammetry of 2 μm thick Ti_3C_2 electrode in 1 M H_2SO_4 vs Hg/Hg_2SO_4 at 10 $mV.s^{-1}$. (b) Bode plots with corresponding fit lines of the effects of electrolyte impregnation on the AC in-plane impedance of Ti_3C_2. (c) DC resistance measurements on Ti_3C_2 in 1 M H_2SO_4 at different applied potentials (*in-situ*). (d) DC resistance measurements on Ti_3C_2 in 1 M H_2SO_4 during cyclic voltametry performed at 5 $mV.s^{-1}$ (*operando*)..

occurs during reduction and oxidation.[6] The similar changes between stationary and dynamic mode, thus confirming the interest of the method for operando tracking of the in-plane electronic resistance change of electrodes for energy storage applications.

Experimental

Carbon electrode preparation.—A solution contained 80% of YP50F and 20% polyvinylidene fluoride (PVDF) in 1-Methyl-2-pyrrolidinone (NMP) was prepared by adding 500 μl of PVDF/NMP (10 mg ml^{-1}) to 20 mg of YP50F. After 10 min stirring and 5 min sonication, the entire solution was sprayed on a polyimide substrate (Kapton©) that was heated to 150 °C. 4 × 4 mm porous carbon electrodes were obtained by placing an overlay a mask onto the Kapton sheet. Au was then sputtered using a Cressington 108 Auto sputtering From Cressington Scientific Instrument (France), at the four corners of the sample using a mask. A representative sample is shown in Fig. 1b.

MXene electrodes preparation.—Single-layer 2D Ti_3C_2 MXene materials were prepared from etching of Ti_3AlC_2 MAX phase in acidic, fluoride containing solutions, as previously reported.[35] Briefly, 1 g of Ti_3AlC_2 was immersed in 20 ml of etchant composed of a 6:3:1 (volume) ratio of hydrochloric acid, deionized (DI) water, and hydrofluoric acid, respectively. Then, the solution was stirred for 24 h at 35 °C. The resulting multilayer Ti_3C_2 was then washed with DI water via repeated centrifugation and decantation of the acidic supernatant until a pH of ~6 was reached. The multilayered Ti_3C_2 was then intercalated with lithium by stirring a suspension of Ti_3C_2 in 50 ml of aqueous solution of 0.5 M LiCl overnight at room temperature (~20 °C). Exfoliation of the lithium intercalated Ti_3C_2 was then induced by repeated washing/centrifugation cycles with DI water until a dark black supernatant of single-layer Ti_3C_2 remained even after 45 min of centrifugation at 3500 rpm. The Ti_3C_2-containing solution was shaken by hand for 10 min between each cycle of centrifugation to aid the exfoliation process.

After filtration, current collector-free Ti_3C_2 electrodes were used to perform the electrochemical measurements (Fig. 1c).

Material characterization.—Electrode thickness was measured using a non-contact 3D optical confocal profiler S-Neox-sensofar microscope (Spain). All samples were electrochemically characterized in 1 M H_2SO_4 using a 3-electrode setup, where the electrode film was the working electrode. A platinum wire was used as counter electrode, and a Hg/Hg_2SO_4 electrode as the reference electrode. Electrochemical characterization, resistance measurements (DC) and in-plane impedance measurements (AC) were performed with a Potentiostat/Galvanostat/ZRA Interface 1010B from GAMRY instruments (United States).

For YP50F in 1 M H_2SO_4, cyclic voltammetry was performed using scan rates from 1 $mV.s^{-1}$ to 10 $mV.s^{-1}$ within a potential range of −0.7 V to +0.2 V vs Hg/Hg_2SO_4. For YP50F in pure EMITFSI, cyclic voltammetry was performed using scan rates of 10 $mV.s^{-1}$ within a potential range of −1.5 V to +1.2 V vs Ag/Ag^+. For Ti_3C_2, cyclic voltammetry was performed at 10 $mV.s^{-1}$ within a potential range from −1.1 V to −0.1 V vs Hg/Hg_2SO_4. All samples were first cycled five times to reach a steady, reproducible electrochemical signature.

Potentiostatic EIS (AC measurement) was performed from 10 kHz to 10 mHz for the activated carbon used in this study and from 10 kHz to 100 mHz for Ti_3C_2 at each applied potential, as the potentiostat used in our experimental set-up had an effective bandwidth of approximately 100 kHz. Gamry software was used to fit the experimental data with an equivalent circuit model.

For porous carbon in 1 M H_2SO_4, classic electrochemical impedance spectroscopy in a three-electrode set-up was performed at different applied potentials (Supplementary Fig. S19), from 10 kHz to 10 mHz. The electrode capacitance (F) at each bias potential was calculated[2] from Eq. 2:

$$C'(\omega) = \frac{-Z''(\omega)}{\omega\,|Z(\omega)|^2} \qquad [2]$$

Where, $\omega = 2\pi f$ (rad.s^{-1}) is the angular frequency, -Z″ is the imaginary part of the impedance (Ω), and $|Z(\omega)|$ is the modulus of the impedance.

Conclusions

Resistance (DC) and in plane impedance measurement (AC) were performed operando on porous carbon (YP50F), and MXene (Ti_3C_2), during electrochemical cycling. Monitoring operando in-plane impedance (AC) has proven to be an effective way to discriminate between the respective impedance contributions of electronic conduction and ionic conduction, which is of particular interest for better understanding the charge storage mechanisms of active materials and in order to guide efforts towards enhancing their performance. Two conduction regimes were found for porous carbon, which has a conductivity in a similar range as the electrolyte: i) a domain corresponding to ionic conduction, which was fairly sensitive to the potential change, and ii) a domain corresponding to electronic conduction, which was strongly correlated to the applied potential. Interestingly, the resistance-potential curve's shape turned out to be dependent on the electrolyte, suggesting changes in charge carrier density and electrode volume with the polarization and the type of electrolyte. Conversely, since the MXene Ti_3C_2 has an overall resistance several orders of magnitude lower than that of the electrolyte, only an electronic resistance was measured. Interestingly, the changes in the MXene's resistance with applied potential was consistent with previous reports on the variation of the *c*-lattice parameter of MXenes during electrochemical cycling. As a result, the changes in the MXene's resistance correlates well with the expansion and contraction of the MXene's interlayer spacing that occurs during oxidation and reduction.

Operando AC in-plane impedance spectroscopy allows for the extraction of valuable data that provides insight regarding the charge transport mechanisms occurring within an active material during cycling. The results presented here are very promising and could be extended to the study of a broader range of active materials for electrochemical energy storage (capacitive materials, pseudo-capacitive materials, or battery-like electrode materials), in a wide variety of electrolytes (aqueous electrolytes, organic electrolytes, and ionic liquids).

Acknowledgments

V. M. was supported by a CNRS PhD grant. P. L. T., T. S. M., and P. S. thank the support of the Agence Nationale de la Recherche (Labex Store-ex) and the ERC Synergy Grant MoMa-Stor #951513.

ORCID

Patrice Simon https://orcid.org/0000-0002-0461-8268

References

1. C. Wang, C. Yang, and Z. Zheng, "Toward practical high-energy and high-power lithium battery anodes: present and future." *Adv. Sci.*, **9**, 2105213 (2022).
2. P. L. Taberna, P. Simon, and J. F. Fauvarque, "Electrochemical characteristics and impedance spectroscopy studies of carbon-carbon supercapacitors." *J. Electrochem. Soc.*, **150**, A292 (2003).
3. K. Brousse, P. Huang, S. Pinaud, M. Respaud, B. Daffos, B. Chaudret, C. Lethien, P. L. Taberna, and P. Simon, "Electrochemical behavior of high performance on-chip porous carbon films for micro-supercapacitors applications in organic electrolytes." *J. Power Sources*, **328**, 520 (2016).
4. K. W. Nam, W. S. Yoon, H. Shin, K. Y. Chung, S. Choi, and X. Q. Yang, "In situ X-ray diffraction studies of mixed $LiMn_2O_4$–$LiNi_{1/3}Co_{1/3}Mn_{1/3}O_2$ composite cathode in Li-ion cells during charge–discharge cycling." *J. Power Sources*, **192**, 652 (2009).
5. P. W. Ruch, M. Hahn, F. Rosciano, M. Holzapfel, H. Kaiser, W. Scheifele, B. Schmitt, P. Novàk, R. Kötz, and A. Wokaun, "In situ X-ray diffraction of the intercalation of $(C_2H_5)_4N^+$ and BF_4^- into graphite from acetonitrile and propylene carbonate based supercapacitor electrolytes." *Electrochim. Acta*, **53**, 1074 (2007).
6. Z. Lin, P. Rozier, B. Duployer, P. L. Taberna, B. Anasori, Y. Gogotsi, and P. Simon, "Electrochemical and in situ X-ray diffraction studies of $Ti_3C_2T_x$ MXene in ionic liquid electrolyte." *Electrochem. Commun.*, **72**, 50 (2016).
7. D. Levi, M. Levy, N. Sigalov, S. Salitra, D. G Aurbach, and J. Maier, "Electrochemical quartz crystal microbalance (EQCM) studies of ions and solvents insertion into highly porous activated carbons." *Journal of the American Chemical Society*, **132**, 13220 (2010).
8. R. Chen et al., "Ultrafast electron transfer kinetics of graphene grown by chemical vapor deposition." *Angew. Chem.*, **54**, 15134 (2015).
9. J. Park, V. Kumar, X. Wang, P. S. Lee, and W. Kim, "Investigation of charge transfer kinetics at carbon/hydroquinone interfaces for redox-active-electrolyte supercapacitors." *ACS Appl. Mater. Interfaces*, **9**, 33728 (2017).
10. G. S. Popkirov, E. Barsoukov, and R. N. Schindler, "Electrochemical impedance spectroscopy of twin working electrodes bridged with conducting polymer layer." *Electrochim. Acta*, **40**, 185 (1995).
11. R. I. Tucceri and D. Posadas, "Theorical approach to the resistive behavior of thin solid film electrodes under direct current polarization." *J. Electrochem. Soc.*, **128**, 1478 (1981).
12. E. Pollak, I. Genish, G. Salitra, A. Soffer, L. Klein, and D. Aurbach, "The dependence of the electronic conductivity of carbon molecular sieve electrodes on their charging states." *J. Phys. Chem. B*, **110**, 7443 (2006).
13. E. Pollak, A. Anderson, G. Salitra, A. Soffer, and D. Aurbach, "The anomaly in the dependence of the electronic conductivity of activated carbon electrodes at different charging states." *J. Electroanal. Chem.*, **601**, 47 (2007).
14. Y. M. Vol'fkovich, A. A. Mikhalin, and A. Y. Rychagov, "Surface conductivity measurements for porous carbon electrodes." *Russ. J. Electrochem.*, **49**, 594 (2013).
15. A. P. Saab, F. H. Garzon, and A. Zawodzinski, "Determination of ionic and electronic resistivities in carbon/polyelectrolyte full-cell composite electrodes." *J. Electrochem. Soc.*, **149**, A1541 (2002).
16. O. Balci, O. Polat, N. E Kakenov, and C. Kocabas, "Graphene-enabled electrically switchable radar-absorbing surfaces." *Nature Commun.*, **6**, 6628 (2015).
17. N. Kakenov, M. S. Ergoktas, O. Balci, and C. Kocabas, "Graphene based terahertz phase modulators." *2D Mater.*, **5**, 035018 (2018).
18. F. Qing et al., "A general and simple method for evaluating the electrical transport performance of graphene by the van der Pauw–Hall measurement." *Sci. Bull.*, **63**, 1521 (2018).
19. S. Matsuo and R. Sottos, "Single carbon fiber transverse electrical resistivity measurement via the van der Pauw method." *Appl. Phys.*, **130**, 115105 (2021).
20. L. J. van der Pauw, "A method of measuring the resistivity and hall coefficient on lamellae of arbitrary shape." *Philips Tech. Rev.*, **20**, 220 (1958).
21. P. Ratajczak, E. Suss M, F. Kaasik, and F. Béguin, "Carbon electrodes for capacitive technologies." *Energy Storage Mater.*, **16**, 126 (2019).
22. C. F. Liu, Y. C. Liu, T. Y. Yi, and C. C. Hu, "Carbon materials for high-voltage supercapacitors." *Carbon*, **145**, 529 (2019).
23. B. Kastening, "A model of the electronic properties of activated carbon." *Ber. Bunsenges. Phys. Chem.*, **102**, 229 (1998).
24. W. Gu and G. Yushin, "Review of nanostructured carbon materials for electrochemical capacitor applications: advantages and limitations of activated carbon, carbide-derived carbon, zeolite-templated carbon, carbon aerogels, carbon nanotubes, onion-like carbon, and graphene." *WIREs Energy Environ*, **3**, 424 (2014).
25. H. Shao, Y. C. Wu, Z. Lin, P. L. Taberna, and P. Simon, "Nanoporous carbon for electrochemical capacitive energy storage." *Chem. Soc. Rev.*, **49**, 3005 (2020).
26. M. Salanne, B. Rotenberg, Naoi K. Kaneko, P. L. K Taberna, C. P. Grey, B. Dunn, and P. Simon, "Efficient storage mechanisms for building better supercapacitors." *Nat. Energy*, **1**, 1 (2016).
27. A. D. Dillon, M. J. Ghidiu, A. L. Krick, J. Griggs, S. J. May, Y. Gogotsi, M. W. Barsoum, and A. T. Fafarman, "Highly conductive optical quality solution-processed films of 2D titanium carbide." *Adv. Funct. Mater.*, **26**, 4162 (2016).
28. K. AlHassoon, M. Han, Y. Malallah, V. Ananthakrishnan, R. Rakhmanov, W. Reil, Y. Gogotsi, and S. Daryoush, "Conductivity extraction of thin $Ti_3C_2T_x$ MXene films over 1–10 GHz using capacitively coupled test-fixture.." *Appl. Phys. Lett.*, **116**, 184101 (2020).
29. J. Zhao et al., "Porous MXene monoliths with locally laminated structure for enhanced pseudo-capacitance and fast sodium-ion storage." *Nano Energy*, **86**, 106091 (2021).
30. Image credit for the electrochemical cell model to: (https://redox.me/products/van-der-pauw-bmm-ec-15-ml-8x8-mm2-van-der-pauw-bottom-magnetic-mount-electrochemical-cell?_pos=1&_sid=efb0a7477&_ss=r). Consulted on 20/10/2021.
31. M. Ender, J. Illig, and E. Ivers-Tiffée, "Three-electrode setups for lithium-ion batteries: i. fem-simulation of different reference electrode designs and their

implications for half-cell impedance spectra." *J. Electrochem. Soc.*, **164**, A71 (2017).
32. F. Kaasik, T. Tamm, M. M. Hantel, E. Perre, A. Aabloo, E. Lust, M. Z. Bazant, and V. Presser, "Anisometric charge dependent swelling of porous carbon in an ionic liquid." *Electrochem. Commun.*, **34**, 196 (2013).
33. M. M. Hantel, D. Weingarth, and R. Kötz, "Parameters determining dimensional changes of porous carbons during capacitive charging." *Carbon*, **69**, 275 (2014).
34. X. Mu, D. Wang, F. Du, G. Chen, C. Wang, Y. Wei, Y. Gogotsi, Y. Gao, and Y. Dall'Agnese, "Revealing the pseudo-intercalation charge storage mechanism of MXenes in acidic electrolyte." *Adv. Funct. Mater.*, **29**, 1902953 (2019).
35. T. S. Mathis, K. Maleski, A. Goad, A. Sarycheva, M. Anayee, C. Foucher, A. Hantanasirisakul, K. E. Shuck, C. A. Stach E, and Y. Gogotsi, "Modified MAX phase synthesis for environmentally stable and highly conductive Ti_3C_2 MXene." *ACS Nano*, **15**, 6420 (2021).